

Wujiu Pan · Xiaopeng Li · Linlin Wang · Na Guo ·
Zemin Yang

Influence of contact stiffness of joint surfaces on oscillation system based on the fractal theory

Received: 26 May 2017 / Accepted: 18 November 2017 / Published online: 27 November 2017
© Springer-Verlag GmbH Germany, part of Springer Nature 2017

Abstract In this paper, in view of microscopic surface topography characteristic, the relationship of microscopic surface topography characteristic and the dynamic characteristic of macroscopic system is established, and the influence of fractal contact stiffness on the stability and nonlinearity of modal coupling system is studied based on microscopic surface topography. According to the fractal characteristic of metal surface machined, the normal and tangential contact stiffness fractal models of joint surfaces are established and verified. In this paper, a critical two-degree-of-freedom modal coupling model is listed, the fractal contact stiffness obtained is embedded into oscillatory differential equation to study the influence of the coupling between friction coefficient and stiffness ratio of joint surfaces and the coupling between natural frequency and stiffness ratio of joint surfaces on the system stability, and the influence of fractal contact stiffness on the limit cycle of system is further analyzed. The above theoretical analysis can provide a reference for the design of suitable surface topography in the engineering.

Keywords Joint surfaces · Contact stiffness · Fractal theory · Oscillation system

1 Introduction

Practice proves that the surface topography and contact behavior of mechanical components have a crucial influence on their properties of wear, fatigue strength, corrosion resistance and so on. The dynamic properties and vibration noise problem of the whole machine system depend on the contact stiffness, contact damping and thermolability to a large extent. Therefore, the estimate and analysis on the dynamic characteristics can make important contribution on promoting the whole property of the mechanical equipment. The rough metal surface machined is characterized by fractal [1,2], that is to say, the partial surface topography and the whole surface topography of surface present the characteristic of self-similarity [3,4], so the fractal theories are usually applied to the three-dimensional description of joint surfaces and contact modeling.

The phenomenon of vibration and noise caused by friction widely exist in the mechanical system, especially the vibration and noise of automotive brake, a rather classical phenomenon, which has been studied for many years. The mechanism study related to the phenomenon is mainly concluded to several mechanisms below: stick-slip theory [5,6], the theory of negative slope of friction force-relative sliding velocity [7], sprag-slip theory [8] and modal coupling theory [9,10].

The dynamic properties of mechanical system should be studied from the perspective of mechanical joint surfaces, and many scholars found that the contact surface topography had an important influence on the

W. Pan · X. Li (✉) · L. Wang · N. Guo · Z. Yang
School of Mechanical Engineering and Automation, Northeastern University, Shenyang 110819, People's Republic of China
E-mail: xpli@me.neu.edu.cn

W. Pan
E-mail: panspace@sina.cn

system vibration and noise by experiments. Eriksson et al. [11] found that the surface topography of brake pad had an important impact on brake squeal, and brake pad with many small asperities was more liable to generate the problem of vibration and noise than that with little large asperities. Chen et al. [12] analyzed the problem of vibration and noise in the process of metal reciprocating sliding from the perspective of tribology, analyzed the surface topography of friction part where the noise appeared, and found that grinding crack had close relationship with noise. Okayama et al. [13] researched the groan noise after the brake and indicated that asperities on the surface of brake pad were the main factor that caused groan noise. The experiment that surface of brake disk was modified indicated that the tendency of brake squeal could be decreased obviously [14]. Rusli et al. [15] built the model of L-shaped beam and studied the influence of contact surface topography on vibration friction characteristics of beam by experiment. Fuadi et al. [16, 17] combined the experimental research with theoretical analysis, and proposed two control conditions that could simplify system: the stiffness ratio and the index of low-frequency stick-slip vibration. When both of two coefficients were greater than a certain limited value, system would generate stick-slip vibration. They also analyzed the change of contact stiffness which perhaps have influence on the appearance or disappearance of creep-groan. Their research ideas and results have important guiding significance.

These literatures above mostly focus on the influence of surface topography of joint surfaces on brake system from the perspective of experiment, but in nature, it is the influence of contact stiffness and damping of joint surfaces on system dynamics. Those previous literatures [9, 10, 18–20] mostly focus on the influence of structural parameters of macroscopic system on vibration and noise, but rarely refer to the perspective of microscopic contact modeling of rough surface, that is to say, firstly, the contact stiffness model of joint surfaces of modal coupling oscillation system is built based on the fractal theory; then, the influence of microscopic fractal contact stiffness on the dynamical properties of system is analyzed. Therefore, this paper aims at building the contact stiffness estimation model of joint surfaces based on fractal theory, starting with microscopic surface topography contact properties, building a bridge between the microscopic surface topography and macroscopic system dynamical properties theoretically.

2 Modeling of contact stiffness

2.1 Critical contact area of asperity

The asperities of rough surface are regarded as spheres, so the contact between two rough planes is regarded as the contact among a series of hemispheroids [21]. As shown in Fig. 1, two asperities generate extrusion deformation under the external force. According to the classical Hertz contact theory, the contact between two asperities is equivalent to the contact between a rigid plane and a rough asperity.

Under the external force, the elastic deformation value of asperity is given by [22]

$$\delta = \left(\frac{3\pi p_a}{4E} \right)^2 R \quad (1)$$

where p_a is the average pressure endured by asperity; E is equivalent elastic modulus, and its expression is Eq. (2); R is equivalent curvature radius of asperity, and its expression is Eq. (3).

$$E = \frac{1}{\left(\frac{1-\nu_1^2}{E_1} + \frac{1-\nu_2^2}{E_2} \right)} \quad (2)$$

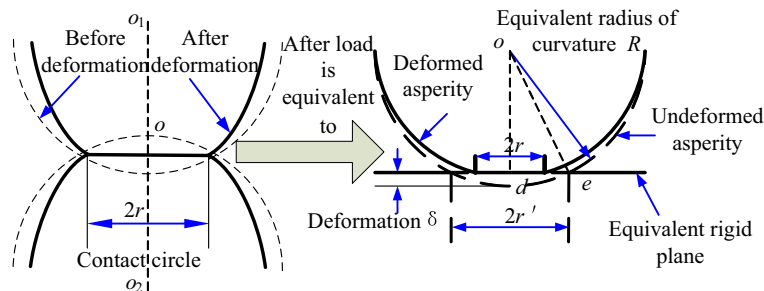


Fig. 1 Equivalent figure of asperity contacting

where E_1 , E_2 and ν_1 , ν_2 are the elastic modulus and Poisson's ratio of two contiguous asperities, respectively.

$$R = \frac{1}{\left(\frac{1}{R_1} + \frac{1}{R_2}\right)} \quad (3)$$

where R_1 , R_2 are the curvature radius of asperity respectively.

In Fig. 1, the cross-sectional area of equivalent asperity and rigid plane is given by

$$A = \pi r'^2 = \pi [R^2 - (R - \delta)^2] \approx 2\pi R\delta \quad (4)$$

In Fig. 1, the right-angled triangle *ode* exists the following relationship by the Pythagorean Theorem, expressed as

$$R^2 = r'^2 + (R - \delta)^2 \quad (5)$$

Equation (5) can be transformed into

$$R = \frac{\delta}{2} + \frac{r'^2}{2\delta} \quad (6)$$

As the R is much larger than the loaded deformation δ , there is $R \gg \delta/2$, and the approximate expression of Eq. (6) is given by

$$R \approx \frac{r'^2}{2\delta} \quad (7)$$

According to Hertz theory, the relation between the load and deformation value of single asperity at the stage of elastic strain is expressed as

$$P_e(\delta) = \frac{4}{3}ER^{0.5}\delta^{1.5} \quad (8)$$

When the asperity is in Hertz elastic contact, the radius r of the actual contact area is given by

$$r = \left(\frac{3P_e R}{4E}\right)^{1/3} \quad (9)$$

Substitution of Eq. (8) into Eq. (9) can obtain

$$r = (R\delta)^{0.5} \quad (10)$$

Substitution of Eq. (7) into Eq. (10) can obtain

$$r = \frac{1}{\sqrt{2}}r' \quad (11)$$

According to the Eqs. (11) and (4), the actual contact area of the equivalent asperity and the equivalent rigid plane is given by

$$a = \pi r^2 = \frac{1}{2}\pi r'^2 = \pi R\delta \quad (12)$$

After being machined, the surface topography of metal is characterized by fractal, so the classic W - M function [23, 25] is used to describe the self-similarity characteristic of surface topography. But it is unreasonable that the two-dimensional fractal curve is used to describe the real three-dimensional surface topography [24]. Given this, Yan and Komvopoulos [25] improved the traditional W - M function to describe three-dimensional fractal surface topography. The improved W - M function is given by

$$z(x, y) = L \left(\frac{G}{L}\right)^{(D-2)} \left(\frac{\ln \gamma}{M}\right)^{1/2} \sum_{m=1}^M \sum_{n=0}^{n_{\max}} \gamma^{(D-3)n} \left\{ \cos \phi_{m,n} - \cos \left[\frac{2\pi \gamma^n (x^2 + y^2)^{1/2}}{L} \times \cos \left(\tan^{-1} \left(\frac{y}{x} \right) - \frac{\pi m}{M} \right) + \phi_{m,n} \right] \right\} \quad (13)$$

where L is the sample length of surface topography; D is the fractal dimension of three-dimensional topography ($2 < D < 3$); G is fractal roughness; D and G are obtained by the measurement of surface topography; γ ($\gamma > 1$, it is generally taken as 1.5) is a parameter that determines the density of frequency; M is the number of

surface peak ridge superposition; n is the frequency index, $n_{\max} = \text{Int} [\log (L/L_s) / \log \gamma]$; L_s is the minimum cut-off length; x and y are the Cartesian coordinate of the surface asperity; $\phi_{m,n}$ is random phase.

In order to determine the deformation value of asperity loaded, Eq. (13) is simplified to Eq. (14) by Yan et al. [25], given by

$$z(x) = G^{D-2}(\ln \gamma)^{0.5}(2r') \left[\cos \phi_{1,n_0} - \cos \left(\frac{\pi x}{r'} - \phi_{1,n_0} \right) \right] \quad (14)$$

The deformation δ of the asperity can be defined by Eq. (14), which is equal to the amplitude difference between peak and trough of the cosine function. That is, when the $\cos \phi_{1,n_0}$ is 1 and $\cos \left(\frac{\pi x}{r'} - \phi_{1,n_0} \right)$ is -1 , we can get the deformation of asperity δ , given by

$$\delta = 2G^{D-2}(\ln \gamma)^{0.5}(2r')^{3-D} \quad (15)$$

Substitute of Eq. (12) into Eq. (15) can obtain

$$\delta = 2^{(11-3D)/2} G^{(D-2)} (\ln \gamma)^{0.5} \pi^{(D-3)/2} a^{(3-D)/2} \quad (16)$$

Substitute of Eq. (16) into Eq. (12) can obtain the curvature radius expressed by area a , given by

$$R = 2^{(3D-11)/2} \pi^{(1-D)/2} G^{(2-D)} a^{(D-1)/2} (\ln \gamma)^{-0.5} \quad (17)$$

When two rough surfaces contacting with each other under oscillating load generate relative slip, the critical contact pressure at the yield of asperity is given by [22,26,27]

$$p_m = 1.1k_\mu \sigma_y \quad (18)$$

where σ_y is the yield strength of softer material; k_μ is a frictional correction factor and its expression is shown below [28].

$$k_\mu = \begin{cases} 1 - 0.228\mu_m & 0 \leq \mu_m \leq 0.3 \\ 0.932 \exp[-1.58(\mu_m - 0.3)] & 0.3 < \mu_m \leq 0.9 \end{cases} \quad (19)$$

where μ_m is dynamic friction coefficient.

Substitute of Eq. (18) into Eq. (1) can obtain the critical elastic deformation of asperity, given by

$$\delta_e = \left(\frac{3.3\pi k_\mu \phi}{4} \right)^2 R \quad (20)$$

where $\phi = \sigma_y/E$ represents characteristic coefficient of material.

According to Eqs. (12), (17) and (20), the critical elastic deformation area of asperity is given by

$$a_e = 2^{(3D-11)/(2-D)} \left(\frac{33k_\mu \phi}{40} \right)^{2/(2-D)} \pi^{(4-D)/(2-D)} (\ln \gamma)^{1/(D-2)} G^2 \quad (21)$$

2.2 Normal contact load of asperity

The plastic average pressure of single asperity under normal load is given by

$$p_{\text{pre}}(\delta) = H \quad (22)$$

where H represents the hardness of softer material.

According to Eq. (22), the normal load of single asperity at the stage of plastic deformation is given by

$$P_p(a) = \lambda \sigma_y a \quad (23)$$

where $\lambda = H/\sigma_y$ is a defined parameter.

Substitute of Eqs. (16) and (17) into Eq. (8) can obtain the elastic contact load expressed by contact area a , given by

$$P_e(a) = \frac{1}{3} E \pi^{(D-4)/2} 2^{(15-3D)/2} (\ln \gamma)^{1/2} G^{D-2} a^{(4-D)/2} \quad (24)$$

2.3 Normal contact stiffness

The relationship between the area distribution function of asperity $n(a)$ [25] of joint surfaces and the maximum contact area of asperity a_1 is expressed as

$$n(a) = \frac{D-1}{2} a_1^{0.5D-0.5} a^{-0.5D-0.5}, 0 < a \leq a_1, 2 < D < 3 \quad (25)$$

The load of single asperity at the stage of elastic deformation and plastic deformation is obtained, respectively, above, and the total normal contact load of whole joint surfaces is the sum of the elastic contact load and plastic contact load.

Therefore, given that the denominator is 0 or not, the classification discussion of total normal contact load equation is conducted. When $a_1 > a_e$ and $D \neq 2.5$, the total normal contact load is given by

$$P = \int_0^{a_e} P_p n(a) da + \int_{a_e}^{a_1} P_e(a) n(a) da = \frac{D-1}{3-D} \lambda \sigma_y a_1^{(D-1)/2} a_e^{(3-D)/2} + \frac{D-1}{15-6D} 2^{(15-3D)/2} E (\ln \gamma)^{1/2} G^{D-2} \pi^{(D-4)/2} a_1^{(D-1)/2} \left(a_1^{(5-2D)/2} - a_e^{(5-2D)/2} \right) \quad (26)$$

When $a_1 > a_e$ and $D = 2.5$, the total normal contact load is given by

$$P = \int_0^{a_e} P_p n(a) da + \int_{a_e}^{a_1} P_e(a) n(a) da = 3 \lambda \sigma_y a_1^{3/4} a_e^{1/4} + \frac{1}{4} E 2^{15/4} \pi^{-3/4} (\ln \gamma)^{1/2} G^{1/2} a_1^{3/4} (\ln a_1 - \ln a_e) \quad (27)$$

The actual contact area A_r of the whole joint surfaces can be obtained by

$$A_r = \int_0^{a_e} n(a) a da + \int_{a_e}^{a_1} n(a) a da = \frac{D-1}{3-D} a_1 \quad (28)$$

According to the definition of stiffness, the normal stiffness of single asperity at the stage of elastic deformation is given by

$$k_n = \frac{dP_e}{d\delta} = \frac{4E}{3\pi^{0.5}} \frac{4-D}{3-D} a^{0.5} \quad (29)$$

According to the distribution function $n(a)$ of the whole surface, the normal contact stiffness of the whole surface is given by

$$K_n = \int_{a_e}^{a_1} k_e n(a) da = \frac{4}{3} \frac{(D-1)(4-D)}{(2-D)(3-D)} E \pi^{-0.5} a_1^{(D-1)/2} \left(a_1^{(2-D)/2} - a_e^{(2-D)/2} \right) \quad (30)$$

The dimensionless form of Eq. (30) is expressed as

$$K_n^* = \frac{4}{3} \frac{(4-D)}{(2-D)} \left(\frac{D-1}{3-D} \right)^{(3-D)/2} \pi^{-0.5} A_r^{*(D-1)/2} \left[\left(\frac{3-D}{D-1} A_r^* \right)^{(2-D)/2} - a_e^{*(2-D)/2} \right] \quad (31)$$

where $K_n^* = K_n / (E \sqrt{A_a})$, $A_r^* = A_r / A_a$, $a_e^* = a_e / A_a$.

2.4 Tangential contact stiffness

According to the study of literature [29], the limit of tangential load of single asperity is given by

$$Q = \frac{8a\sigma_y}{(6-3\nu)\pi} + \frac{8(2\nu-1)}{\pi(6-3\nu)}P \quad (32)$$

At the stage of fully plastic flow, asperity cannot bear tangential load, so in the process of calculating the total tangential load of asperity, the elastic deformation is only considered.

According to Eqs. (25) and (32), when $D \neq 2.5$, the tangential load is given by

$$\begin{aligned} Q_e &= \int_{a_e}^{a_1} \left[\frac{8a}{\pi(6-3\nu)}\sigma_y + \frac{8(2\nu-1)}{\pi(6-3\nu)}P_e \right] n(a) da \\ &= \frac{8(D-1)\sigma_y}{\pi(3-D)(6-3\nu)} a_1^{(D-1)/2} \left(a_1^{(3-D)/2} - a_e^{(3-D)/2} \right) \\ &\quad + \frac{8(D-1)(2\nu-1)E}{3(5-2D)(6-3\nu)} 2^{(15-3D)/2} \pi^{(D-6)/2} (\ln \gamma)^{1/2} G^{D-2} a_1^{(D-1)/2} \left[a_1^{(5-2D)/2} - a_e^{(5-2D)/2} \right] \end{aligned} \quad (33)$$

When $D = 2.5$, the tangential load is given by

$$Q_e = \frac{24\sigma_y}{\pi(6-3\nu)} a_1^{3/4} \left(a_1^{1/4} - a_e^{1/4} \right) \frac{(2\nu-1)E}{(6-3\nu)} 2^{19/4} \pi^{-7/4} (\ln \gamma)^{1/2} G^{1/2} a_1^{3/4} (\ln a_1 - \ln a_e) \quad (34)$$

The tangential contact stiffness of single asperity is expressed as [30,31]

$$k_t = \frac{8\bar{G}\sqrt{a}}{(2-\nu)\sqrt{\pi}} \left(1 - \frac{1}{\mu} \frac{Q_e}{P} \right)^{1/3} \quad (35)$$

Similarly, according to Eqs. (25) and (35), the tangential contact stiffness of the whole joint surfaces is expressed as

$$K_t = \int_{a_e}^{a_1} k_t n(a) da = \frac{8\bar{G}(D-1)}{\sqrt{\pi}(2-D)(2-\nu)} \left(1 - \frac{1}{\mu} \frac{Q_e}{P} \right)^{1/3} a_1^{(D-1)/2} \left[a_1^{(2-D)/2} - a_e^{(2-D)/2} \right] \quad (36)$$

where \bar{G} is equivalent elastic shear modulus, $\bar{G} = \frac{E}{2(1+\nu)}$.

The dimensionless form of Eq. (36) is expressed as

$$\begin{aligned} K_t^* &= \frac{8}{\sqrt{\pi}(2-\nu)(2+2\nu)} \frac{(D-1)^{(3-D)/2} (3-D)^{(D-1)/2}}{2-D} \left(1 - \frac{1}{\mu} \frac{Q_e^*}{P^*} \right)^{1/3} \\ &\quad \times A_r^{*(D-1)/2} \left[\left(\frac{3-D}{D-1} A_r^* \right)^{(2-D)/2} - a_e^{*(2-D)/2} \right] \end{aligned} \quad (37)$$

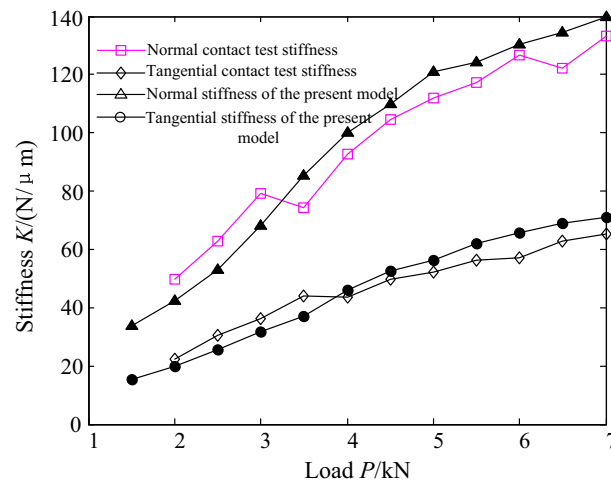
where $K_t^* = K_t / (\bar{G}\sqrt{A_a})$, $Q_e^* = Q_e / (EA_a)$, $P^* = P / (EA_a)$.

2.5 Model validation and simulation

Equations (30) and (36) represent the normal stiffness and tangential stiffness deduced based on the fractal theory, respectively. In order to verify the accuracy of the two models, they are compared with the test results in the literature [32] where the normal stiffness and tangential stiffness of machine tool support joints are studied. The main test methods in literature [32] are as follows: firstly, the binding site of the machine's supporting foundation is equivalent to spring damping system of three directions, and it is dynamics modeled, then the modal frequency and damping ratio of the bed are obtained by modal test, and finally, the equivalent stiffness of the binding site of the machine's supporting foundation is identified. In order to identify any supported state

Table 1 Parameters of machine tool support joints

Parameter	Value
Equivalent elastic modulus E/Pa	1.1538×10^{11}
Poisson's ratio ν	0.3
Fractal dimension D	2.4241
Fractal roughness G/m	5.1372×10^{-5}
Yield strength σ_y/Pa	2.35×10^8
Scale parameters γ	1.5

**Fig. 2** Comparison of theoretical and experimental curves

of the foundations, the positive pressure of foundation is changed, so we can get the test stiffness curves under different loads. The material is carbon steel Q235, the mass is 2800 kg, the elastic modulus is $E = 2.1 \times 10^{11}$ Pa, the hardness is $H = 1.96 \times 10^9$ Pa, and the Poisson's ratio is $\nu = 0.3$. These two important fractal parameters of the rough surface are the fractal dimension D and the fractal roughness G , and they can be obtained by the power spectral density (PSD) function method. The surface topography is measured by the T1000 stylus profilometer whose lateral resolution is $0.6 \mu\text{m}$ and the stylus radius is $2 \mu\text{m}$. The sampling length is 10 mm. The contour curve obtained is analyzed by the PSD analysis, then the two-dimensional fractal dimension $D_s = 1.4241$, and the fractal roughness $G = 5.1372 \times 10^{-5}$ m are obtained. The three-dimensional fractal dimension [24] is expressed as $D = D_s + 1$. The concrete engineering parameters are shown in Table 1. When the external load is $P = 2.5$ kN, the parameters in Table 1 are substituted into Eqs. (21), (26) and (30) to obtain the normal stiffness $K_n = 5.282 \times 10^7$ N/m. The different external load P corresponds to different K_n . The same can be done for the tangential stiffness. The theoretical curves of different stiffness data in MATLAB R2014a are compared with the experimental curves in literature [32]. As shown in Fig. 2, the overall trend of the theoretical prediction is consistent with that of the experimental test and their results are close, so we can build the whole system dynamical model based on the fractal stiffness model.

In order to obtain the changing trend of dimensionless normal and tangential contact stiffness with fractal dimension D and dimensionless fractal roughness G^* ($G^* = G/\sqrt{A_a}$), according to Eqs. (31) and (37), the simulation relationship diagram can be obtained.

As shown in Figs. 3 and 4, with D and G^* increasing, the dimensionless normal contact stiffness and tangential contact stiffness tend to monotonically increase and decrease, respectively. That the larger D means more high frequency components of three-dimensional surface topography so the surface is much finer in the macroscopic view; that the larger G^* means amplitude of three-dimensional surface topography is larger so the surface is more rough. The reason is that the surface is more smooth, the actual contact area is much larger, and the contact stiffness is much larger. On the contrary, the surface is more rough, the actual contact area is much smaller, and the contact stiffness is much smaller.

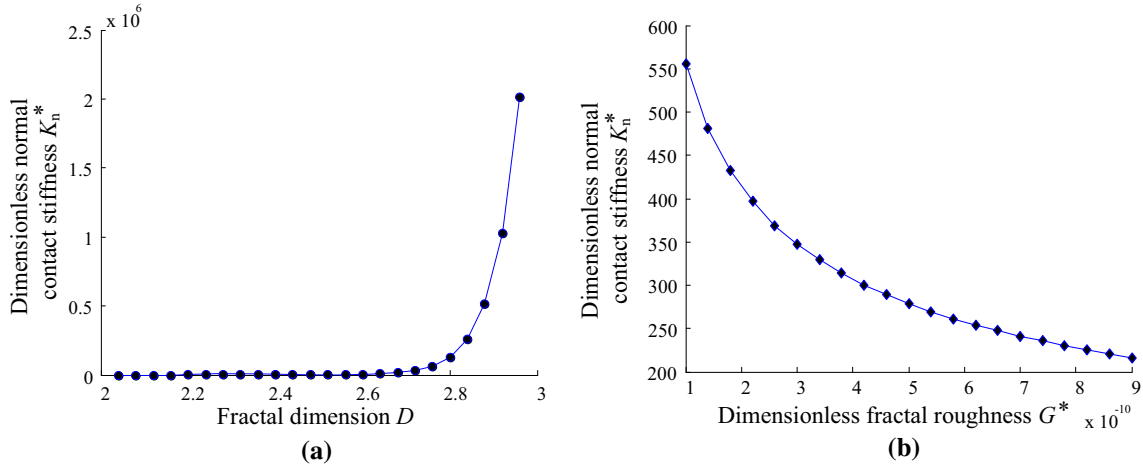


Fig. 3 Relationship between dimensionless normal contact stiffness and fractal dimension, fractal roughness, respectively. **a** The relationship between D and K_n^* . **b** The relationship between G^* and K_n^*

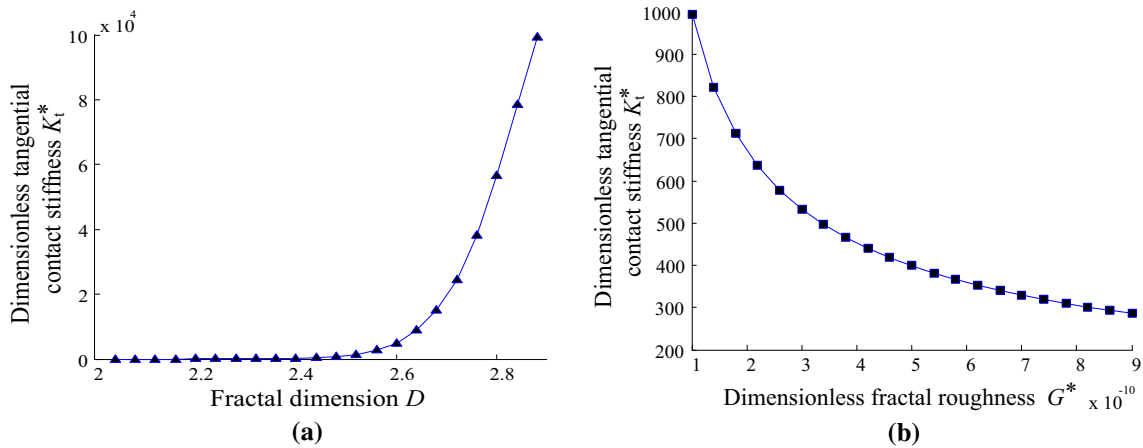


Fig. 4 Relationship between dimensionless tangential contact stiffness and fractal dimension, fractal roughness respectively. **a** The relationship between D and K_t^* . **b** The relationship between G^* and K_t^*

3 Model of oscillation system

3.1 Physical model

In order to study the influence of contact stiffness on self-excited system based on fractal theory, a two-degree-of-freedom mass-belt system is studied and its physical model is shown in Fig. 5. The model is firstly used to study the vibration and noise of drum brake by Hultén [33,34]; then, it is used to study the influence of damping on system by Sinou et al. [10,18,19]. In this paper, the models of literatures [10,18,19,33,34] are slightly improved. In Fig. 5, K_1 , K_2 and C_1 , C_2 are the stiffness and damping of system, respectively; K_n and K_t are the fractal contact stiffness and fractal tangential contact stiffness, respectively, which can be obtained by the first section. The system includes the external force F , the angle α , which is 45° , and the speed of belt V . The mass block is always in contact with the belt in the x_1 and x_2 direction under the force F . In order to simplify problems, the literatures [9,10] assume that the direction of friction is constant. But actually the direction of friction is variable and the simplification may lead to the neglect of nonlinear characteristic caused by changing the direction of friction. Given this, in this paper, the Stribeck friction model between the mass block and belt which is widely applied to the contact modeling is considered [35–37].

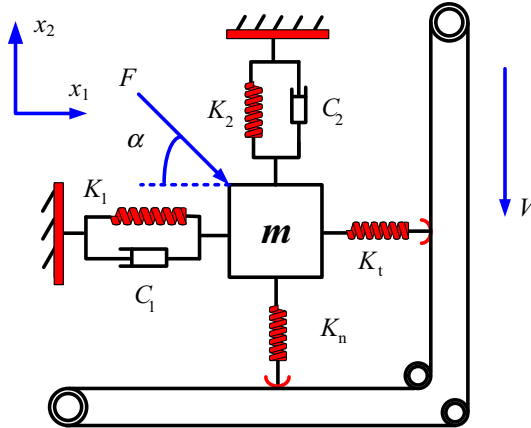


Fig. 5 Self-excited oscillation system

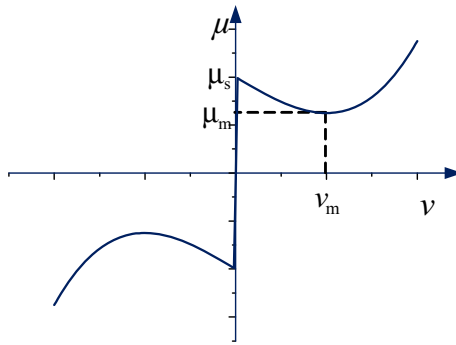


Fig. 6 Stribeck friction model

The expression of Stribeck friction model is shown below.

$$\mu(v_r) = \mu_s \operatorname{sgn}(v_r) - \frac{3(\mu_s - \mu_m)}{2v_m} v_r + \frac{(\mu_s - \mu_m)}{2v_m^3} v_r^3 \quad (38)$$

where $\mu(v_r)$ is friction factor, v_r is the relative sliding speed, μ_s is the corresponding friction factor when $v_r=0$, (v_m, μ_m) represents the minimum point of friction curve. In Fig. 6, the curve corresponding to $v_r < 0$ shows that the direction of friction changes with the relative sliding speed changing.

As shown in Fig. 5, the dynamic equation of the system is given by

$$M\ddot{X} + C\dot{X} + KX = F \quad (39)$$

where $M = \begin{bmatrix} m & 0 \\ 0 & m \end{bmatrix}$, $C = \begin{bmatrix} C_1 & 0 \\ 0 & C_2 \end{bmatrix}$, $K = \begin{bmatrix} K_1 + K_t & 0 \\ 0 & K_2 + K_n \end{bmatrix}$, $F = \begin{bmatrix} \frac{\sqrt{2}}{2}F + \mu(v_1)K_n x_2 \\ -\frac{\sqrt{2}}{2}F - \mu(v_2)K_t x_1 \end{bmatrix}$, $X = \begin{bmatrix} x_1 \\ x_2 \end{bmatrix}$, $v_i = V - \dot{x}_i, (i = 1, 2)$.

In Fig. 5, the external force F can cause static displacement of system. When $\ddot{x}_1 = \ddot{x}_2 = 0, \dot{x}_1 = \dot{x}_2 = 0$, the static equilibrium point of the whole system is expressed as:

$$x_{01} = \frac{\frac{\sqrt{2}}{2}F(K_2 + K_n) - \frac{\sqrt{2}}{2}FK_n(\mu_s - \kappa_1 V + \kappa_2 V^3)}{(K_2 + K_n)(K_1 + K_t) + K_t K_n(\mu_s - \kappa_1 V + \kappa_2 V^3)^2}, x_{02} = \frac{(K_1 + K_t)x_{01} - \frac{\sqrt{2}}{2}F}{K_n(\mu_s - \kappa_1 V + \kappa_2 V^3)} \quad (40)$$

Setting the static balance point as the new coordinate origin and substitute of $x'_1 = x_1 - x_{01}$, $x'_2 = x_2 - x_{02}$ into Eq. (39) can obtain the following equation.

$$\begin{aligned} & \begin{bmatrix} m & 0 \\ 0 & m \end{bmatrix} \begin{bmatrix} \ddot{x}'_1 \\ \ddot{x}'_2 \end{bmatrix} + \begin{bmatrix} C_1 & 0 \\ 0 & C_2 \end{bmatrix} \begin{bmatrix} \dot{x}'_1 \\ \dot{x}'_2 \end{bmatrix} + \begin{bmatrix} K_1 + K_t & -\mu(v_1)K_n \\ \mu(v_2)K_t & K_2 + K_n \end{bmatrix} \begin{bmatrix} x'_1 \\ x'_2 \end{bmatrix} \\ & = \begin{bmatrix} \frac{\sqrt{2}}{2}F - (K_1 + K_t)x_{01} + \mu(v_1)K_n x_{02} \\ -\frac{\sqrt{2}}{2}F - \mu(v_2)K_t x_{01} - (K_2 + K_n)x_{02} \end{bmatrix} \end{aligned} \tag{41}$$

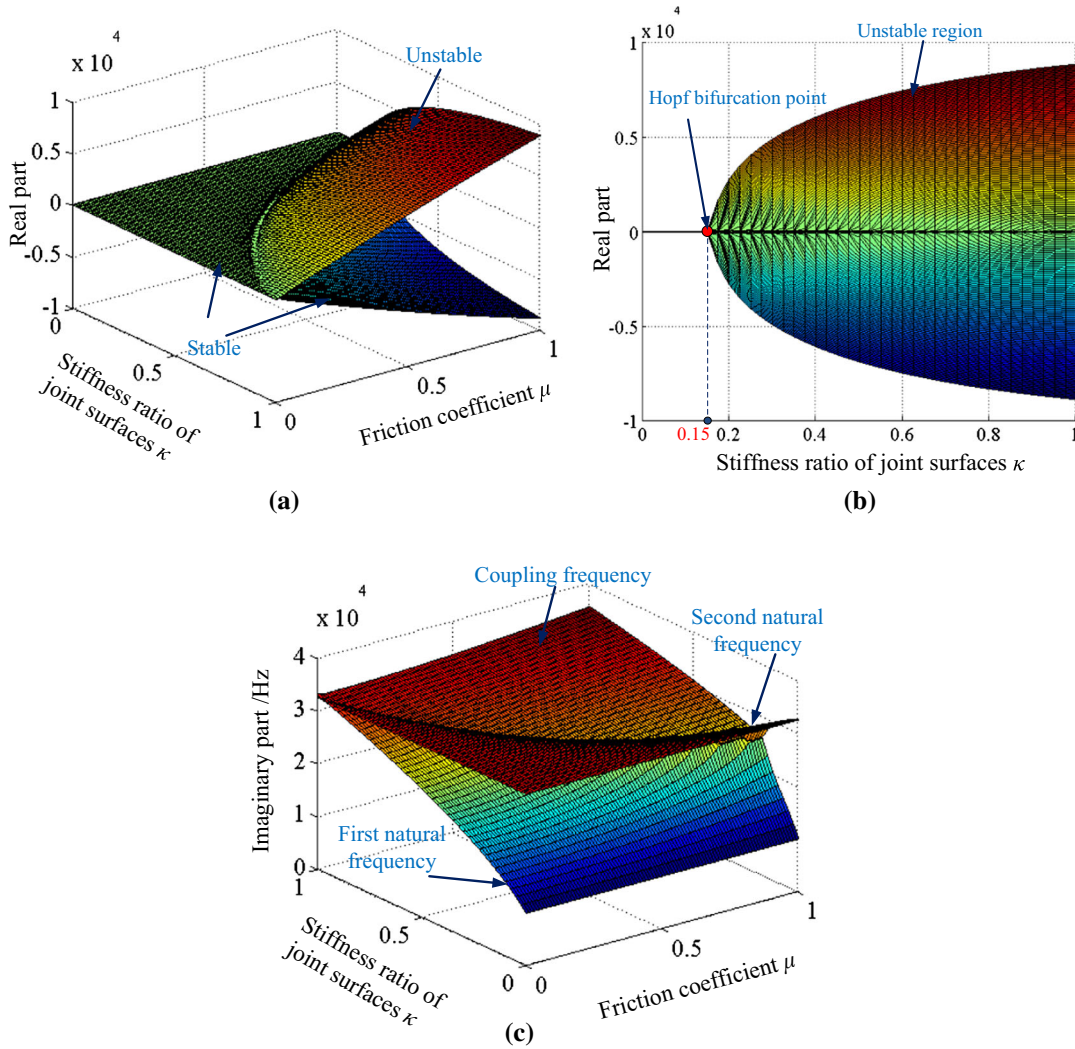


Fig. 7 Influence of friction coefficient and stiffness ratio of joint surfaces on stability. **a** Influence of friction coefficient and stiffness ratio on real part. **b** Relationship between stiffness ratio and real part. **c** Influence of friction coefficient and stiffness ratio on imaginary part

3.2 Stability analysis

Given the homogeneous form of Eq. (41), it is linearly processed to obtain

$$\begin{bmatrix} m & 0 \\ 0 & m \end{bmatrix} \begin{bmatrix} \ddot{x}'_1 \\ \ddot{x}'_2 \end{bmatrix} + \begin{bmatrix} C_1 & 0 \\ 0 & C_2 \end{bmatrix} \begin{bmatrix} \dot{x}'_1 \\ \dot{x}'_2 \end{bmatrix} + \begin{bmatrix} K_1 + K_t - \mu(v_1)K_n & \\ \mu(v_2)K_t & K_2 + K_n \end{bmatrix} \begin{bmatrix} x'_1 \\ x'_2 \end{bmatrix} = \begin{bmatrix} 0 \\ 0 \end{bmatrix} \quad (42)$$

The both sides of Eq. (42) are divided by mass m , and the damping ratio is defined as $\xi_i = \frac{C_i}{2\omega_i m}$ ($i = 1, 2$), and the natural frequency is defined as $\omega_i^2 = \frac{K_i}{m}$ ($i = 1, 2$).

$$\begin{bmatrix} 1 & 0 \\ 0 & 1 \end{bmatrix} \begin{bmatrix} \ddot{x}'_1 \\ \ddot{x}'_2 \end{bmatrix} + \begin{bmatrix} 2\xi_1\omega_1 & 0 \\ 0 & 2\xi_2\omega_2 \end{bmatrix} \begin{bmatrix} \dot{x}'_1 \\ \dot{x}'_2 \end{bmatrix} + \begin{bmatrix} \omega_1^2 + \frac{K_t}{m} & \frac{-\mu(v_1)K_n}{m} \\ \frac{\mu(v_2)K_t}{m} & \omega_2^2 + \frac{K_n}{m} \end{bmatrix} \begin{bmatrix} x'_1 \\ x'_2 \end{bmatrix} = \begin{bmatrix} 0 \\ 0 \end{bmatrix} \quad (43)$$

In the process of analyzing stability of system, according to complex modal analysis theory, the real part of eigenvalue \Re of system is greater than zero, which shows that the system is unstable; otherwise, the system is stable.

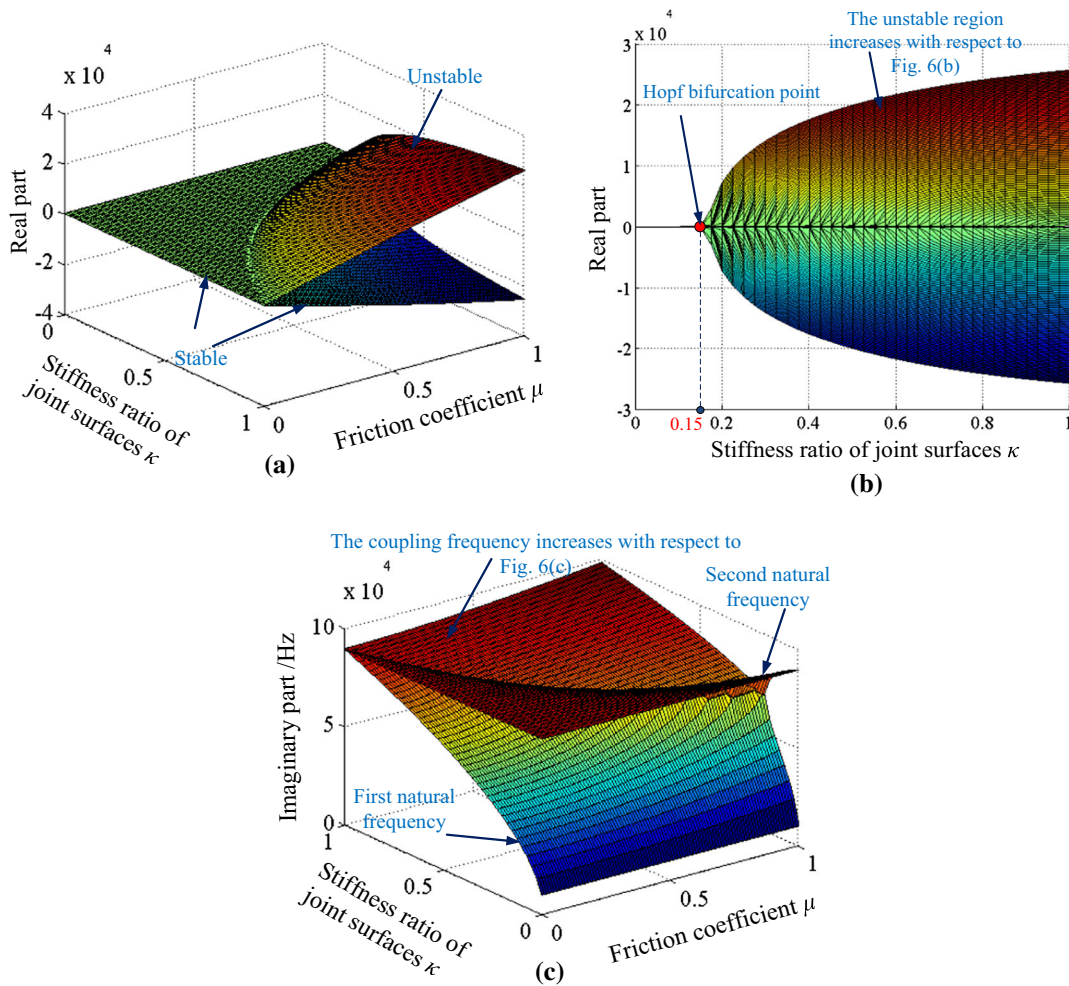


Fig. 8 Influence of friction coefficient and stiffness ratio of joint surfaces on stability ($8K_n$). **a** Influence of friction coefficient and stiffness ratio on real part. **b** Relationship between stiffness ratio and real part. **c** Influence of friction coefficient and stiffness ratio on imaginary part

3.2.1 Influence of friction coefficient and stiffness ratio of joint surfaces on stability

In order to reveal the influence of the contact stiffness determined by the surface topography parameters on the stability and nonlinearity of the system, we adopt the following parameters to carry out simulation analysis. Setting $m = 1 \text{ Kg}$, $\omega_1 = 2000\pi \text{ rads}^{-1}$, $\omega_2 = 1600\pi \text{ rads}^{-1}$, $\xi_1 = 0.001$, $\xi_2 = 0.007$. K_n is normal contact stiffness based on the fractal theory, and $K_n = 4 \times 10^8 \text{ N/m}$ can be obtained by these given parameters, $D = 2.4$, $G = 1.342 \times 10^{-8} \text{ m}$, $E = 1.154 \times 10^{11} \text{ Pa}$, $\nu = 0.3$, $\sigma_y = 3.55 \times 10^8 \text{ Pa}$, $\gamma = 1.5$, $P = 1.9073 \times 10^3 \text{ N}$, and Eqs. (26) and (30). The ratio of tangential stiffness to normal stiffness of joint surfaces is defined as the stiffness ratio κ . Figure 7 shows the relationship among characteristic real part (growth rate), friction coefficient μ and stiffness ratio κ . Figure 8 shows the relationship among characteristic imaginary part (frequency), friction coefficient μ and stiffness ratio κ . The normal contact stiffness in Fig. 8 is eight times bigger than that in Fig. 7. As shown in Figs. 7a and 8a, that the real part is greater than zero indicates unstable region in which brake disk usually generates the vibration and noise. The unstable region of system corresponds to coupling frequencies region in Figs. 7c and 8c. The lower layer is the first natural frequency of system, the higher layer is the second natural frequency of system, and they gradually tend to coupling with μ and κ increasing. When κ is smaller and μ is larger, the system is liable to generate lower frequency noise; when κ is larger and μ is smaller, the system is liable to generate higher frequency noise. When the normal contact stiffness increases by a factor of eight, the changing trends of Figs. 7 and 8 are nearly the same, but according to their own y-axis, the coupling frequency and the area of unstable region obviously increase with the normal stiffness increasing. With K_n changing, Hopf bifurcation point ($\kappa = 0.15$) is changeless.

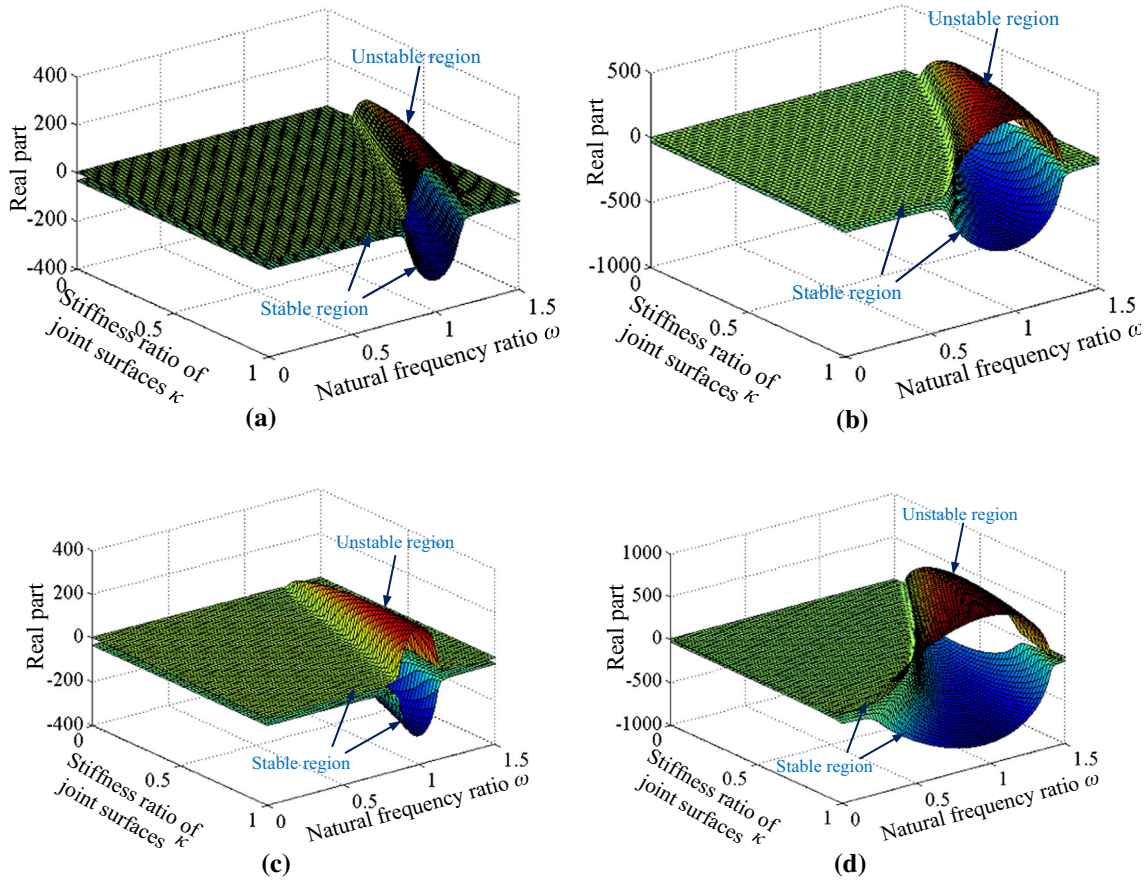


Fig. 9 Influence of natural frequency ratio and stiffness ratio of joint surfaces on real part. **a** $\mu = 0.1$, $K_n = 4 \times 10^8 \text{ N/m}$. **b** $\mu = 0.2$, $K_n = 4 \times 10^8 \text{ N/m}$. **c** $\mu = 0.2$, $K_n = \frac{2}{5} \times 4 \times 10^8 \text{ N/m}$. **d** $\mu = 0.3$, $K_n = 4 \times 10^8 \text{ N/m}$

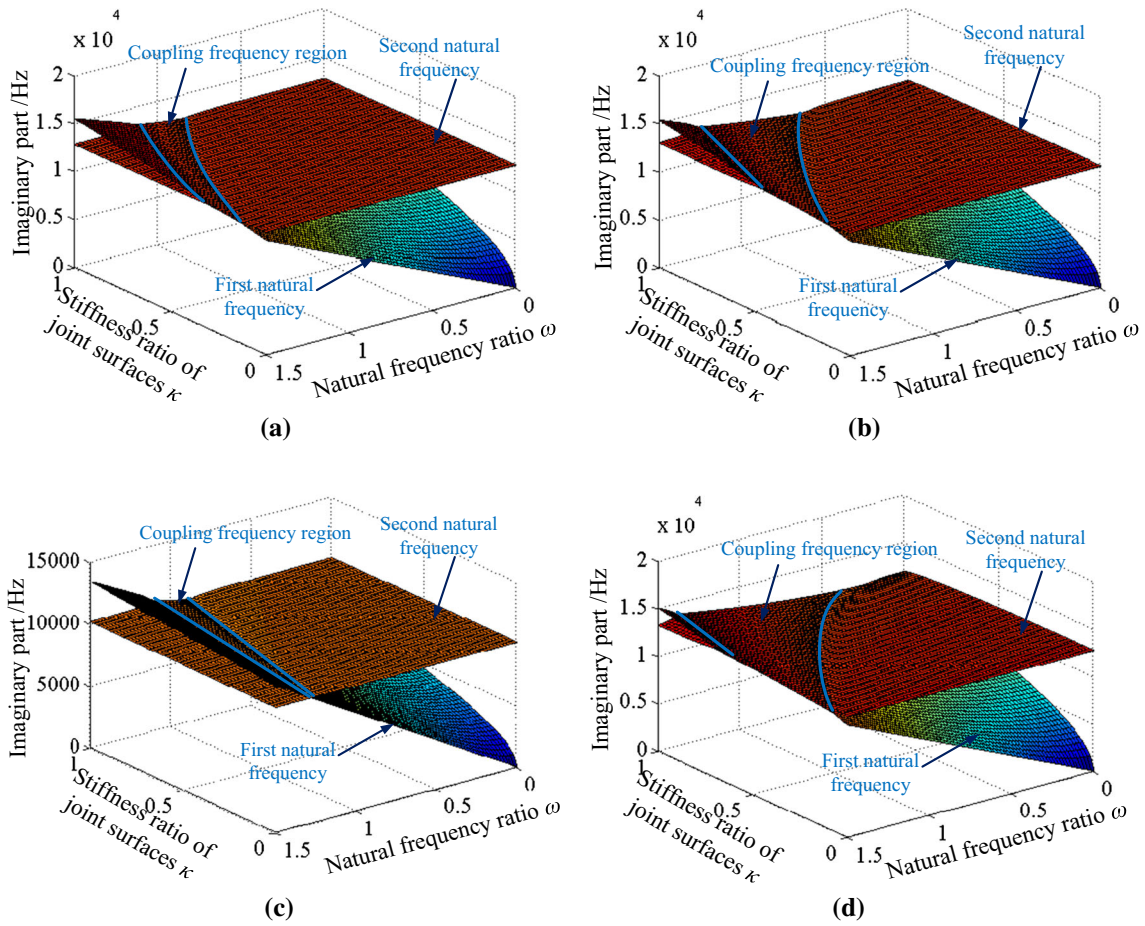


Fig. 10 Influence of natural frequency ratio and stiffness ratio of joint surfaces on imaginary part. **a** $\mu = 0.1$, $K_n = 4 \times 10^8$ N/m. **b** $\mu = 0.2$, $K_n = 4 \times 10^8$ N/m. **c** $\mu = 0.2$, $K_n = \frac{2}{3} \times 4 \times 10^8$ N/m. **d** $\mu = 0.3$, $K_n = 4 \times 10^8$ N/m

3.2.2 Influence of natural frequency ratio and stiffness ratio of joint surfaces on stability

In order to further study the influence of coupling between the stiffness ratio of joint surfaces determined by rough surface topography and the natural frequency ratio ($\omega = \omega_1/\omega_2$) determined by system parameter on stability, four groups of parameters are given to study the evolution process of the real part and imaginary part of system eigenvalue. Other parameters are the same as those in Sect. 3.2.1. As shown in Fig. 9c and d, with μ and K_n increasing, the unstable region of system increases and the relevant stable region decreases. As shown in Fig. 9a and c, with μ increasing and K_n decreasing, the change of unstable region of the whole system is not obvious. As shown in Fig. 9a, b and c, with μ increasing and changeless K_n , the area of unstable region increases. Seen from all four figures, with ω and κ gradually increasing, the change trends of the system in turn are stability, instability and stability. That the smaller ω and larger κ is prone to make system unstable; that the larger ω and smaller κ is also prone to make system unstable. Figure 10 shows the change of characteristic imaginary part corresponding to Fig. 9. The comparison between Fig. 10b and c shows that the first and second natural frequencies both decrease; the comparison among Fig. 10a, b and d shows their change are both not obvious. In addition, the coupling frequency of system increases with ω and κ increasing.

3.3 Nonlinear analysis

In order to further know the influence of contact stiffness on oscillation system dynamics based on fractal theory, the Eq. (44) will be handled by 4–5 order Runge–Kutta method to obtain the nonlinear behavior properties below.

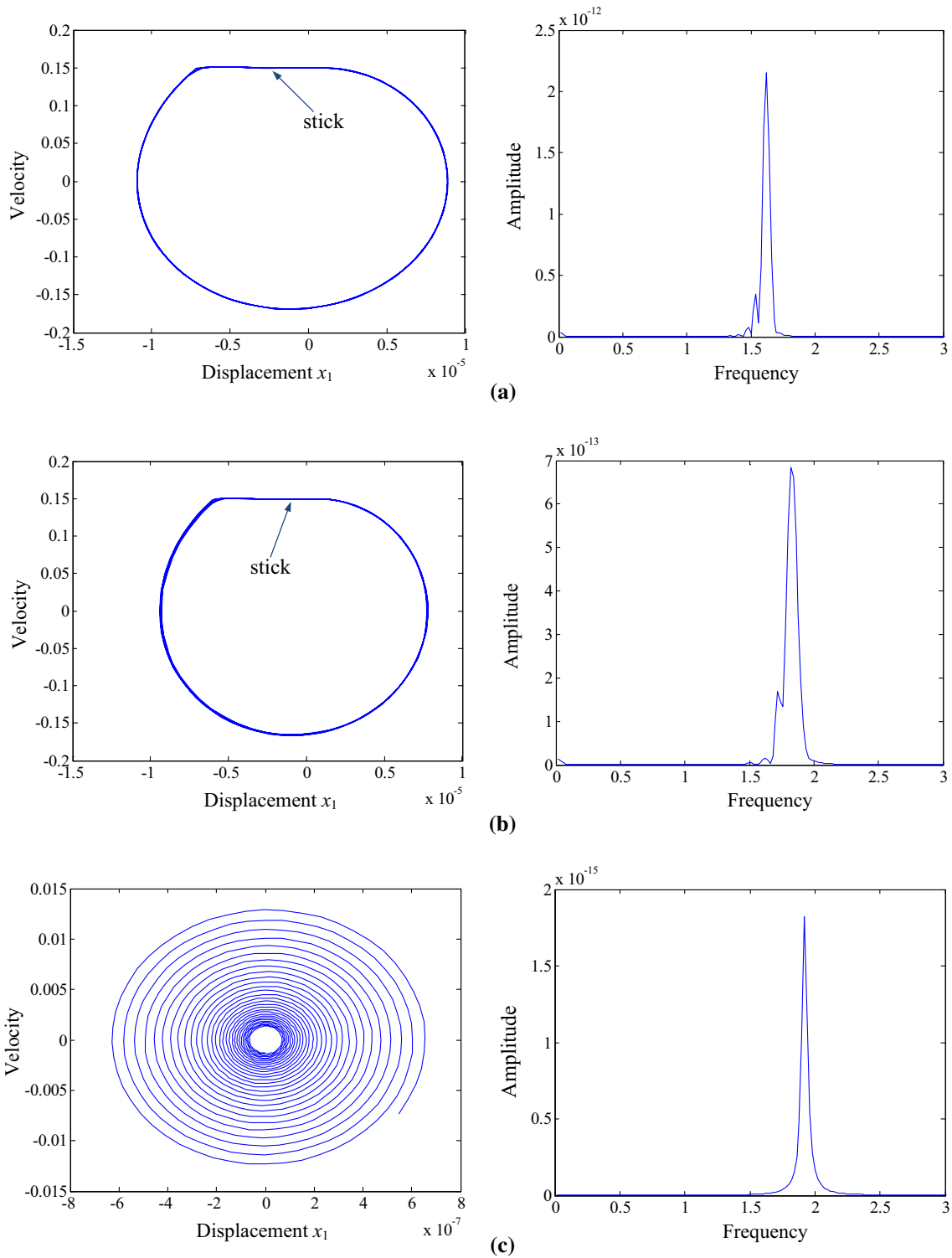


Fig. 11 Nonlinear analysis in horizontal vibration direction. **a** Phase diagram and frequency spectrum with $K_n = 3e8$ N/m. **b** Phase diagram and frequency spectrum with $K_n = 4e8$ N/m. **c** Phase diagram and frequency spectrum with $K_n = 5e8$ N/m

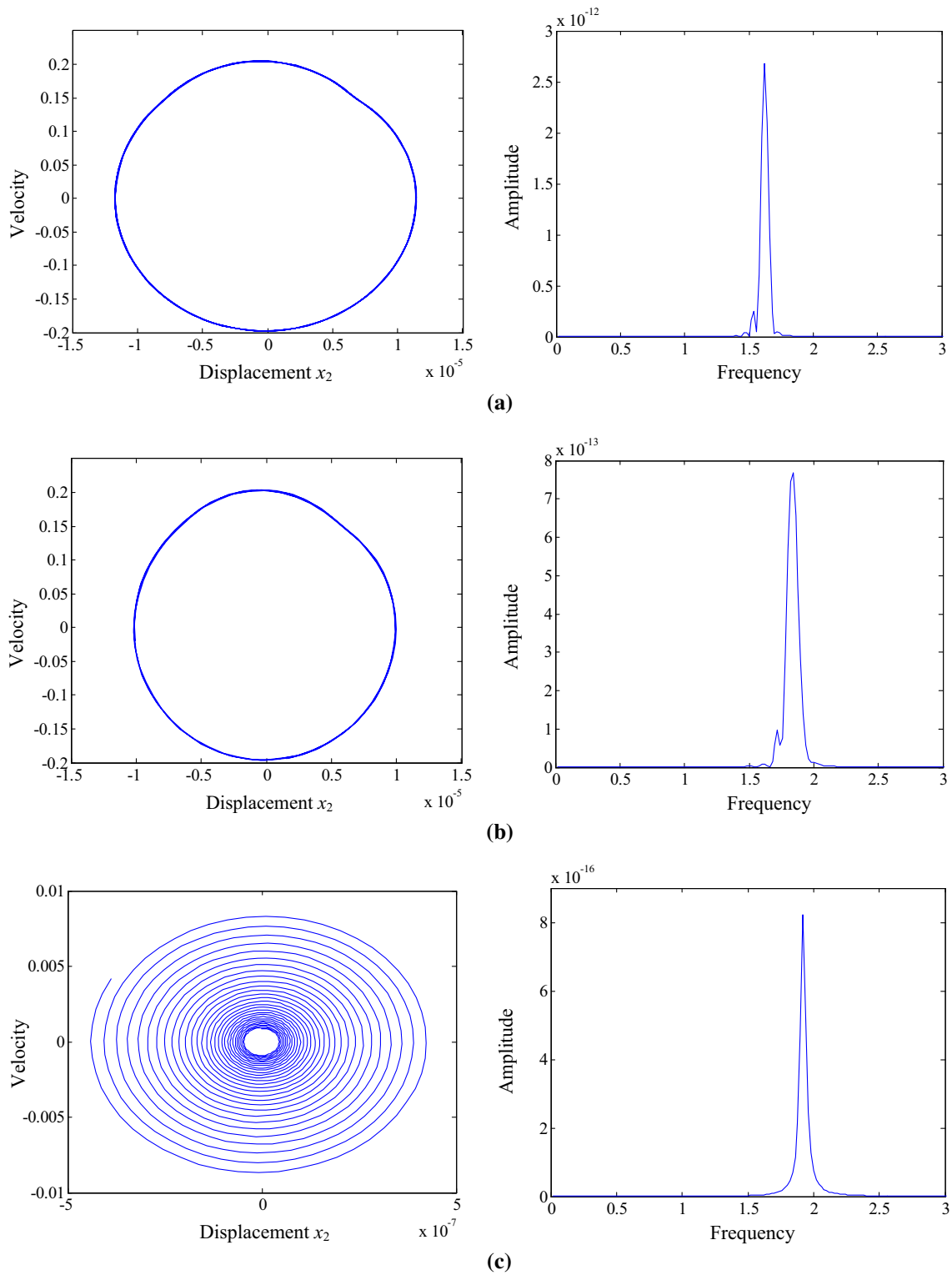


Fig. 12 Nonlinear analysis in vertical vibration direction. **a** Phase diagram and frequency spectrum with $K_n = 3e8$ N/m. **b** Phase diagram and frequency spectrum with $K_n = 4e8$ N/m. **c** Phase diagram and frequency spectrum with $K_n = 5e8$ N/m

$$\begin{aligned}
& \begin{bmatrix} 1 & 0 \\ 0 & 1 \end{bmatrix} \begin{bmatrix} \ddot{x}'_1 \\ \ddot{x}'_2 \end{bmatrix} + \begin{bmatrix} 2\xi_1\omega_1 & 0 \\ 0 & 2\xi_2\omega_2 \end{bmatrix} \begin{bmatrix} \dot{x}'_1 \\ \dot{x}'_2 \end{bmatrix} + \begin{bmatrix} \omega_1^2 + \frac{K_t}{m} & -\frac{\mu(v_1)K_n}{m} \\ \frac{\mu(v_2)K_t}{m} & \omega_2^2 + \frac{K_n}{m} \end{bmatrix} \begin{bmatrix} x'_1 \\ x'_2 \end{bmatrix} \\
& = \begin{bmatrix} \frac{\sqrt{2}}{2} \frac{F}{m} - \left(\omega_1^2 + \frac{K_t}{m}\right) x_{01} + \frac{\mu(v_1)K_n}{m} x_{02} \\ -\frac{\sqrt{2}}{2} \frac{F}{m} - \frac{\mu(v_2)K_t}{m} x_{01} - \left(\omega_2^2 + \frac{K_n}{m}\right) x_{02} \end{bmatrix} \quad (44)
\end{aligned}$$

Here, we mainly observe and analyze phase diagram and frequency spectrum of self-excited system to study the influence of different contact stiffness on system dynamics. Some parameters are given below, $V = 0.15$ m/s, $\mu_s = 0.4$, $\mu_m = 0.25$, $v_m = 0.5$ m/s, $F = 5$ N, $\kappa = 0.5$, the value of other parameters are shown in part 3.2.1.

As shown in Fig. 11, self-excited vibration of the system is divided into stick-slip motion and pure sliding. When the stick-slip motion happens, there will be a rather obvious viscous stage (horizontal line of phase diagram) in the limit cycle, and at the viscous stage, the relative speed between mass block and belt is zero. When the pure sliding happens, the relative speed between them is not zero all the time because viscous stage does not exist in phase diagram.

In addition, with normal contact stiffness of joint surfaces increasing, the ratio of viscous stage to oscillation system decreases; when K_n increases to a certain limit, the viscous stage will disappear, and the system enters the stable pure sliding stage. As shown in frequency spectrum, with K_n increasing, subharmonic disappears and resonant amplitude decreases.

Therefore, the contact stiffness of joint surfaces increases to some extent (by increasing fractal dimension D and decreasing fractal roughness G), which reduces the viscous motion to promote the system stability.

As shown in Fig. 12, in vertical direction, the limit cycle of system decreases with K_n increasing and in the whole change process, it presents the pure sliding motion.

According to the analysis of Figs. 11 and 12, the surface topography between brake joint surfaces need to be specially studied and machined to obtain appropriate fractal dimension D and fractal roughness G . And eventually D and G are used to calculate the contact stiffness. Appropriate contact stiffness of joint surfaces can promote the stability of system.

4 Conclusions

In this paper, the influence of surface topography of joint surfaces on a classical modal coupling system is studied in theory. But as for the vibration and noise caused by inappropriate surface topography, how to avoid this phenomenon in the practical engineering still needs to be completed continuously in theory and experiment, and needs to be further explored. The main conclusions are shown below.

1. The normal and tangential contact stiffness models of joint surfaces are established based on the fractal theory, and the fractal contact stiffness can provide the basis for dynamical modeling of the whole system. The normal and tangential contact stiffness of relative smooth surface (fractal dimension D is larger) are both larger than those of relative rough surface (fractal roughness G is larger).
2. When κ is smaller and μ is larger, system tends to generate lower noise; when κ is larger and μ is smaller, system tends to generate higher noise; with the normal contact stiffness increasing, the coupling frequency and unstable area both increase obviously; that the smaller ω and larger κ is liable to make system unstable; that the larger ω and smaller κ is also liable to make system unstable; with ω and κ increasing, the coupling frequency of system increases.
3. That the fractal dimension D increases and the fractal roughness G decreases can increase the contact stiffness of joint surfaces to promote the stability of system.

Acknowledgements The authors greatly appreciate the reviewers' suggestions and the editor's encouragement. This work was supported, in part, by a Grant from National Natural Science Foundation of China (Nos. 51275079 and 51575091) and Fundamental Research Funds for the Central Universities (N160306003).

References

1. Majumdar, A., Tien, C.L.: Fractal characterization and simulation of rough surfaces. *Wear* **136**, 313–327 (1990)

2. Majumdar, A., Bhushan, B.: Fractal model of elastic–plastic contact between rough surfaces. *ASME J. Tribol.* **113**, 1–11 (1991)
3. Zhang, X., Jackson, R.L.: An analysis of the multiscale structure of surfaces with various finishes. *Tribol. Trans.* **60**, 121–134 (2016)
4. Zhang, X., Xu, Y., Jackson, R.L.: An analysis of generated fractal and measured rough surfaces in regards to their multi-scale structure and fractal dimension. *Tribol. Int.* **105**, 94–101 (2017)
5. Ibrahim, R.A.: Friction-induced vibration, chatter, squeal, and chaos—part I: mechanics of contact and friction. *ASME Appl. Mech. Rev.* **47**, 209–226 (1994)
6. Hunstig, M., Hemsell, T., Sextro, W.: High-velocity operation of piezoelectric inertia motors: experimental validation. *Arch. Appl. Mech.* **86**, 1733–1741 (2016)
7. Ibrahim, R.A.: Friction-induced vibration, chatter, squeal, and chaos—part II: dynamics and modeling. *ASME Appl. Mech. Rev.* **47**, 227–235 (1994)
8. Spurr, R.T.: A theory of brake squeal. *Proc. Inst. Mech. Eng. Auto.* **1961**, 33–52 (1961)
9. Hoffmann, N., Gaul, L.: Effects of damping on mode-coupling instability in friction induced oscillations. *ZAMM. J. Appl. Maths. Mech.* **83**, 524–534 (2003)
10. Sinou, J.J., Jézéquel, L.: Mode coupling instability in friction-induced vibrations and its dependency on system parameters including damping. *Eur. J. Mech.- A/Solids* **26**, 106–122 (2007)
11. Eriksson, M., Bergman, F., Jacobson, S.: Surface characterisation of brake pads after running under silent and squealing conditions. *Wear* **232**, 163–167 (1999)
12. Chen, G.X., Zhou, Z.R., Li, H., Liu, Q.Y.: Profile analysis related to friction-induced noise under reciprocating sliding conditions. *Chin. J. Mech. Eng.* **38**, 85–88 (2002)
13. Okayama, K., Fujikawa, H., Kubota, T., Kakihara, K.: A study on rear disc brake groan noise immediately after stopping. In: 23rd Annual Brake Colloquium and Exhibition. Orlando SAE 2005-01-3917 (2005)
14. Hammerström, L., Jacobson, S.: Surface modification of brake discs to reduce squeal problems. *Wear* **261**, 53–57 (2006)
15. Rusli, M., Okuma, M.: Squeal noise prediction in dry contact sliding systems by means of experimental spatial matrix identification. *J. Syst. Des. Dyn.* **2**, 585–595 (2008)
16. Fuadi, Z., Adachi, K., Ikeda, H., Naito, H., Kato, K.: Effect of contact stiffness on creep-groan occurrence on a simple caliper-slider experimental model. *Tribol. Lett.* **33**, 169–178 (2009)
17. Fuadi, Z., Maegawa, S., Nakano, K., Adachi, K.: Map of low-frequency stick-slip of a creep groan. *Proc. Inst. Mech. Eng. J J. Eng. Tribol* **224**, 1235–1246 (2010)
18. Sinou, J.J., Jézéquel, L.: The influence of damping on the limit cycles for a self-exciting mechanism. *J. Sound & Vib.* **304**, 875–893 (2007)
19. Sinou, J.J., Fritz, G., Jézéquel, L.: The role of damping and definition of the robust damping factor for a self-exciting mechanism with constant friction. *J. Vib. Acoust.* **129**, 297–306 (2007)
20. Charroyer, L., Chiello, O., Sinou, J.J.: Parametric study of the mode coupling instability for a simple system with planar or rectilinear friction. *J. Sound Vib.* **384**, 94–112 (2016)
21. Greenwood, J.A., Tripp, J.H.: The elastic contact of rough spheres. *J. Appl. Mech.* **34**, 153–159 (1967)
22. Johnson, K.L.: *Contact Mechanics*. Cambridge University Press, Cambridge (1985)
23. Ge, S.R., Zhu, H.: *Tribology Fractal*. Machinery Industry Press, Beijing (2005)
24. Liou, J.L., Lin, J.F.: A new microcontact model developed for variable fractal dimension, topography, density of asperity, and probability density function of asperity heights. *ASME J. Appl. Mech.* **74**, 603–613 (2007)
25. Yan, W., Komvopoulos, K.: Contact analysis of elastic–plastic fractal surfaces. *J. Appl. Phys.* **84**, 3617–3624 (1998)
26. Li, X.P., Yue, B., Zhao, G.H., Sun, D.H.: Fractal prediction model for normal contact damping of joint surfaces considering friction factors and its simulation. *Adv. Mech. Eng.* **2014**, 1–5 (2014)
27. Li, X.P., Liang, Y.J., Zhao, G.H., Ju, X., Yang, H.T.: Dynamic characteristics of joint surface considering friction and vibration factors based on fractal theory. *J. Vibroeng.* **15**, 872–883 (2013)
28. Sackfield, A., Hills, D.A.: Some useful results in the tangentially loaded Hertzian contact problem. *Strain Anal.* **18**, 107–110 (1983)
29. Sheng, X.Y., Luo, J.B., Wen, S.Z.: Prediction of static friction coefficient based on fractal contact. *China Mech. Eng.* **9**, 16–18 (1998)
30. Wen, S.H., Zhang, X.L., Wen, X.G., Wang, P.Y., Wu, M.X.: Fractal model of tangential contact stiffness of joint interfaces and its simulation. *Trans. Chinese Soc. Agric. Mach.* **40**, 223–227 (2009)
31. Zhang, X.L., Wang, N.S., Lan, G.S., Wen, S.H., Chen, Y.H.: Tangential damping and its dissipation factor models of joint interfaces based on fractal theory with simulations. *ASME J. Tribol.* **136**, 011704–011710 (2014)
32. Zhang, H., Yu, C.L., Wang, R.C., Ye, P.Q., Liang, W.Y.: Parameters identification method for machine tool support joints. *J. Tsinghua Univ. (Sci. Technol.)* **54**, 815–821 (2014)
33. Hultén, J.: Drum brake squeal—a self-exciting mechanism with constant friction. In: *SAE Truck and Bus Conference Detroit*, pp. 695–706. (1993)
34. Hultén, J.: Friction phenomena related to drum brake squeal instabilities. In: *ASME design engineering technical conferences. Sacramento*, pp. 588–596. (1997)
35. Riebe, S., Ulbrich, H.: Modelling and online computation of the dynamics of a parallel kinematic with six degrees-of-freedom. *Arch. Appl. Mech.* **72**, 817–829 (2003)
36. Hua, C., Rao, Z., Na, T., Zhu, Z.: Nonlinear dynamics of rub-impact on a rotor-rubber bearing system with the Stribeck friction model. *J. Mech. Sci. Tech.* **29**, 3109–3119 (2015)
37. Jiang, H., Jiang, W.: Study of lateral-axial coupling vibration of propeller-shaft system excited by nonlinear friction. *Arch. Appl. Mech.* **86**, 1537–1550 (2016)